A Geometry and Synchronization Error Decoupling and Compensation Approach for Multistatic SAR Imaging

Wanmin Wu, *Student Member, IEEE*, Wei Pu, *Member, IEEE*, Junjie Wu, *Senior Member, IEEE*, Yu Hai, *Student Member, IEEE*, Xinyu Mao, *Student Member, IEEE*, Hongyang An, *Member, IEEE*, and Zhongyu Li, *Member, IEEE*

***Abstract*—Increasing the synthetic aperture radar (SAR) imaging frame rate is vital for obtaining continuous SAR images and dynamic scene monitoring, which multistatic SAR can achieve. Multiple source synchronization errors in multistatic SAR enable the image to produce positional offset and target defocus, which deteriorate the image quality. In order to obtain highly precise multistatic SAR images, synchronization errors must be compensated for. However, geometry errors are unavoidable during platform movement, which introduce Doppler frequency errors and range cell migration just like synchronization errors. Therefore, these two errors will jointly affect the imaging quality when coupled together, which will increase the difficulty of compensation. Aiming to resolve the issue of obtaining imaging results when the two errors exist simultaneously, this article proposes a decoupled estimation and compensation method for geometry and synchronization error. At first, the coupling relationship between geometry error and synchronization error on echo delay and Doppler frequency is analyzed. Next, the decoupled estimation problem with geometry and synchronization error is transformed into a constrained optimization problem. Then, the differential evolutionary algorithm is employed to address the optimization problem. Finally, the estimated values are utilized to compensate for the echoes to obtain high-resolution imaging results, which are verified by the simulation results. The experimental results convincingly demonstrate the improvement of the proposed method in imaging frame rate and error decoupling ability.**

***Index Terms*—Differential evolution (DE) algorithm, error decoupling, geometry error, multistatic synthetic aperture radar (SAR), synchronization error.**

I. Introduction

SYNTHETIC aperture radar (SAR) is an all-weather, all-day, high-resolution imaging radar with a high azimuthal resolution based on aperture synthesis [1], [2], [3], [4], [5], which is widely used in both military and civil fields [6], [7]. The increased frame rate of SAR imaging enables continuous dynamic imaging of the ground scene of interest for surveillance purposes [8], [9], [10], [11], especially in imaging a moving target. However, improving the imaging frame rate implies a short synthetic aperture length, which makes it challenging to obtain azimuthal high resolution for airborne platforms. The platform motion speed or carrier frequency can be increased to improve azimuthal high resolution and imaging frame rate simultaneously. However, monostatic high-frame rate SAR requires high operating carrier frequencies, such as THz band, due to the platform speed limitation [9], [12].

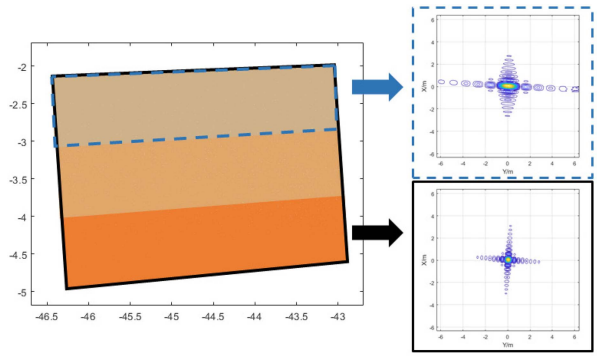

Fig. 1. Concatenation of the spatial spectra of the echoes from each receiver.

To resolve this problem, a high frame rate SAR imaging approach under a microwave band is proposed by [13], which divides the subapertures to enable multiple unmanned aerial vehicles (UAV) to realize the imaging of each subaperture in a short time separately, eventually fusing all subimages to realize azimuthal high-resolution imaging. Thus, a larger aperture is synthesized with a shorter flight time, improving the imaging frame rate while achieving azimuthal high-resolution imaging [14]. As shown in Fig. 1, based on multistatic SAR, it is feasible to utilize the distribution of subapertures corresponding to different transceiver combinations on the spatial spectrum to equate monostatic large aperture observation.

However, the separated platforms in a multistatic SAR system will inevitably cause specific errors in the clock calibration and frequency source between platforms, leading to the introduction of time-frequency synchronization error in the echo, which can bring about problems such as target position drift, main lobe widening, and side lobe lifting in the imaging results [15], [16],

Received 2 June 2024; revised 15 July 2024; accepted 30 July 2024. Date of publication 7 August 2024; date of current version 6 September 2024. *(Corresponding author: Wei Pu.)*

The authors are with the School of Information and Communication Engineering, University of Electronic Science and Technology of China, Chengdu 611731, China (e-mail: wanminw5@163.com; pwuestc@163.com; junjie_wu@uestc.edu.cn; hyuestcarticle@163.com; 445328760@qq.com; hongyang_an@uestc.edu.cn; zhongyu_li@uestc.edu.cn).

Digital Object Identifier 10.1109/JSTARS.2024.3439876

[17]. Traditional methods of compensating synchronization errors by direct waveform will increase system complexity and limit configurations, which brings difficulties to compensating the synchronization error [18]. In addition, the synchronization error is coupled with the geometry error, making it challenging to compensate for both concurrently.

Numerous researchers have proposed various methods to estimate the geometry error or synchronization error, respectively [19], [20], [21], [22]. Aiming at the geometry error caused by the inaccuracy of aerial position, [23] estimates the residual motion errors (RME) by dividing multiple subapertures, and the motion error of the subapertures is modeled as a linear error for estimation compensation. Li et al. [24] considered all errors as spatial variants and the Doppler phase was extracted to estimate the actual motion trajectory and compensate for the echo. To address the instability of UAV flying for a long time, Luomei and Xu [25] divided the motion trajectory of the UAV into uneven segments, with each segment considered to be linear and stable, then compensated the geometry error for each segment to obtain the focused image separately, which were finally stitched together to form a complete image. Against synchronization error, a time-frequency synchronization error solution is proposed in [26] for distributed SAR from the waveform design point of view by using waveforms composed of two linear frequency modulation (FM) signals with different frequencies to achieve unidirectional telesynchronization. Li et al. [27] eliminated the slope due to distance traveling by trapezoidal transformation followed by iterative estimation of the remaining slope to estimate the linear time synchronization error. Wang et al. [28] coarsely compensated the time and frequency synchronization error by direct wave and then built an optimization model based on the image entropy to search for and compensate for the residual synchronization error without compensating the geometric error. However, the aforementioned approaches are used to estimate and compensate for synchronization error or geometry error individually. When these two errors are coupled, the estimation methods for individual errors are not applicable, so they can only be estimated separately.

Aiming at this challenge, this article proposes a geometry and synchronization error decoupled estimation and compensation method for multistatic SAR imaging. The echo characteristics of multistatic SAR, including the range cell migration and Doppler parameters, as well as the impacts of geometry error and synchronization error on them, are analyzed initially. On this basis, the constrained optimization problem for estimating the error is derived based on the coupling of the two errors. First of all, the effects of the existence of geometry error and synchronization error on the echo characteristics are investigated to deduce the expressions for components of the theoretical value, geometry error, and synchronization error in the actual Doppler frequency and time delay to obtain the coupling relationship between geometry error and synchronization error. Afterwards, according to the actual values of Doppler frequency and time delay and the expressions of each component, the decoupling model of geometry error and synchronization error is established and optimized by utilizing the differential evolution (DE) algorithm to search for the optimal solutions of these two types of errors, which is aimed at realizing the practical decoupling estimation of geometry error and synchronization error. Eventually, the phase factors are constructed to compensate the echo depending on the optimization results of geometry and synchronization error. The back-projection (BP) algorithm is used to obtain well-focused imaging results, followed by the fusion of all the subimages to obtain azimuthal high-resolution imaging results with frame rate enhancement.

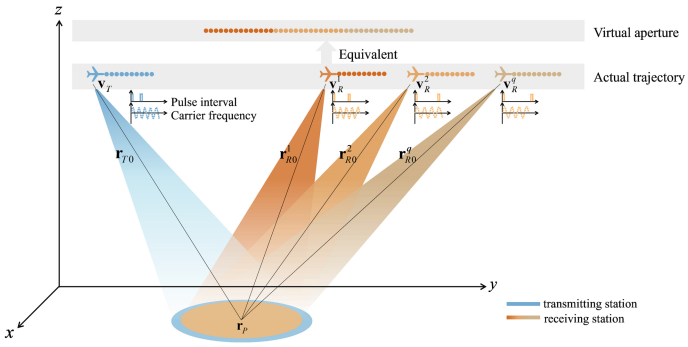

Fig. 2. Multistatic SAR configuration.

The rest of this article is organized as follows. In Section II, the characteristics of Doppler frequency and time delay are analyzed based on the ones-transmitter-multireceiver multistatic SAR model to obtain the coupling relationship between the synchronization error and geometry error. The optimization model and its solution method for error decoupling are proposed in Section III. Section IV presents and analyzes the simulation results. Finally, Section V concludes this article.

II. Signal Model and Characteristic

In this section, a multistatic SAR echo model coupled with geometry error and synchronization error is developed to analyze the characteristics of the two types of error and their effects on the echo.

Fig. 2 gives a multistatic SAR model in the one-transmitter-multireceiver mode, which consists of a formation of $Q+1$ stations, where a blue station transmits echoes with the center moment position coordinate $\mathbf{r}_{T0}=[x_{T0},y_{T0},z_{T0}]$ and a flight velocity of $\mathbf{v}_T=[v_{Tx},v_{Ty},v_{Tz}]$, the remaining orange stations have the same velocity as the transmitting station to receive echoes. The center moment position coordinate of the qth receiver is $\mathbf{r}_{R0}^q=[x_{R0}^q,y_{R0}^q,z_{R0}^q]$, with flight velocity $\mathbf{v}_R^q=[v_{Rx}^q,v_{Ry}^q,v_{Rz}^q]$. The coordinate of any scattering point P in the center of the scene is $\mathbf{r}_p=[x_P,y_P,z_P]$. In this model, the reflected waves of the transmitted beam are received simultaneously by Q receivers, respectively.

For the synchronization error by to separated platforms, Li et al. [29] discussed the baseband echo model of point P by the qth receiving station that incorporated both time and frequency synchronization error. When the movement of platform introduces geometry error, then the echo is denoted as

$$s^q(\tau,\eta;\mathbf{r}_p)=\operatorname{rect}\left(\frac{\Delta t^q(\eta)+\tau-R^q(\eta;\mathbf{r}_p)/\mathrm{c}}{T_r}\right)^{\langle 1\rangle}$$

$$\cdot \exp\left\{ j\pi K_r \left[\Delta t^q(\eta) + \tau - \frac{R^q(\eta;\mathbf{r}_p)}{\mathrm{c}} \right]^2 \right\}^{\langle 2 \rangle}$$
$$\cdot \exp\left[-j2\pi f_c \frac{R^q(\eta;\mathbf{r}_p)}{\mathrm{c}} \right]^{\langle 3 \rangle}$$
$$\cdot \exp[-j2\pi \Delta f^q(\eta)\eta] \cdot \exp[-j2\pi \Delta f^q(\eta)\tau]^{\langle 4 \rangle}$$
$$\cdot \exp\left[-j2\pi \Delta f^q(\eta)\Delta t_0\right]^{\langle 5 \rangle} \quad (1)$$

where c is the speed of light, τ and η stand for the fast time and slow time, severally. $\mathrm{rect}(\cdot)$ is rectangular window function, f_c is the carrier frequency, and K_r means the range FM rate. $R^q(\eta;\mathbf{r}_p)$ is the range history between the transmitter and the $q(q=1,2,\ldots,Q)$th receiver. $\Delta t^q(\eta)$ and $\Delta f^q(\eta)$ are time and frequency synchronization errors, respectively, represented as

$$\begin{cases} \Delta f^q(\eta) = f_c\mu_0^q + f_c\mu_1^q\eta + f_c\mu_2^q\eta^2 + o(\eta) \\ \Delta t^q(\eta) = \Delta t_0 - \mu_0^q - \dfrac{1}{2}\mu_1^q\eta - \dfrac{1}{3}\mu_2^q\eta^2 + o(\eta) \end{cases} \quad (2)$$

where Δt_0 is the time deviation between two different platforms, μ_0^q, μ_1^q, and μ_2^q are the constant, linear, and quadratic frequency reference errors separately.

In (1), range window $\langle 1 \rangle$ and phase term $\langle 2 \rangle$ represent the effects of time synchronization error and geometry errors. $\langle 3 \rangle$ is the Doppler phase introduced by actual range history. $\langle 4 \rangle$ and $\langle 5 \rangle$ indicate the effect of frequency synchronization errors on the Doppler phase; the latter causes a loss of bandwidth along the fast time dimension for the pulse compression process, however, the fast time bandwidth loss is usually very marginal compared to the bandwidth of transmitted signal, and while $\langle 6 \rangle$ is tiny, so both are negligible. Therefore, ignoring random noise and target backscattered coefficients, the pulse-compressed echo model of the qth receiving station with geometry error and synchronization error coupling can be expressed as

$$s_{rc}^q(\tau,\eta;r_p) = \rho_r\left[\tau - \left(\frac{R_e^q(\eta;\mathbf{r}_p)}{c} - \Delta t^q(\eta)\right)\right] \cdot \exp\left\{-j2\pi f_c \frac{R_e^q(\eta;\mathbf{r}_p)}{c}\right\} \cdot \exp\left\{-j2\pi \Delta f^q(\eta)\eta\right\} \quad (3)$$

where $\rho_r(\cdot)$ is range envelope and $R_e^q(\eta;\mathbf{r}_p)$ is actual range history, which is represented as

$$\begin{aligned} R_e^q(\eta;\mathbf{r}_p) &= R_{Te}^q(\eta;\mathbf{r}_p) + R_{Re}^q(\eta;\mathbf{r}_p) \\ &= \|\mathbf{r}_{Te}(\eta) - \mathbf{r}_p\| + \|\mathbf{r}_{Re}^q(\eta) - \mathbf{r}_p\| \\ &= \|\mathbf{r}_{T0} + \mathbf{v}_T\eta - \mathbf{r}_p\| + \|\mathbf{r}_{R0}^q + \mathbf{v}_R\eta - \mathbf{r}_p\| \end{aligned} \quad (4)$$

where $\|\cdot\|$ is the Euclidean norm, $\mathbf{r}_{Te}(\eta)$ and $\mathbf{r}_{Re}^q(\eta)$, respectively, denotes the actual trajectories of transmitter and receiver. Owing to the existence of geometry error, the relationship between actual trajectories and ideal trajectories $\mathbf{r}_T(\eta)$ and $\mathbf{r}_R^q(\eta)$ can be expressed as follows:

$$\begin{cases} \mathbf{r_{Te}}(\eta) = \mathbf{r_T}(\eta)\mathbf{\Phi}(\alpha_\mathbf{T})\mathbf{\Psi}(\beta_\mathbf{T}) + \mathbf{\Delta e_T} \\ \mathbf{r}_{Re}^q(\eta) = \mathbf{r}_R^q(\eta)\Phi(\alpha_R^q)\Psi(\beta_R^q) + \Delta e_R^q \end{cases} \quad (5)$$

where Δe_T and Δe_R^q are error constant coordinates as well as $\Phi(\alpha)$ and $\Psi(\beta)$ denote the rotation matrices corresponding to the error azimuth α and pitch angle β, respectively, which is denoted as

$$\begin{cases} \Phi(\alpha) = \begin{bmatrix} \cos\alpha & -\sin\alpha & 0 \\ \sin\alpha & \cos\alpha & 0 \\ 0 & 0 & 1 \end{bmatrix} \\ \Psi(\beta) = \begin{bmatrix} 1 & 0 & 0 \\ 0 & \cos\beta & -\sin\beta \\ 0 & \sin\beta & \cos\beta \end{bmatrix} \end{cases}. \quad (6)$$

The direction of the velocity will change, but the magnitude will remain the same. A Taylor expansion of the range history yields the expression

$$R_e^q(\eta;\mathbf{r}_p) = \left\|\mathbf{r}_{T_pe0}\right\| + \left\|\mathbf{r}_{R_pe0}^q\right\| + \sum_{n=1}^{\infty}\frac{1}{n!}\left(k_{nTe} + k_{nRe}\right)\eta^n \quad (7)$$

where R_{Te0} and R_{Re0}^q are the actual instantaneous slant ranges of the transmitter and the qth receiver at the beam center crossing time, and

$$\left\|\mathbf{r}_{T_pe0}\right\| = \left\|\mathbf{r}_{Te0} - \mathbf{r}_p\right\|, \left\|\mathbf{r}_{R_pe0}^q\right\| = \left\|\mathbf{r}_{Re0}^q - \mathbf{r}_p\right\| \quad (8)$$

$$k_{1Te} = \frac{\mathbf{v}_{Te}\cdot\mathbf{r}_{T_pe0}}{\left\|\mathbf{r}_{T_pe0}\right\|}, k_{1Re}^q = \frac{\mathbf{v}_{Re}^q\cdot\mathbf{r}_{R_pe0}^q}{\left\|\mathbf{r}_{R_pe0}^q\right\|} \quad (9)$$

$$k_{2Te} = \frac{\|\mathbf{v}_{Te}\|^2 - k_{1Te}^2}{\left\|\mathbf{r}_{T_pe0}\right\|}, k_{2Re}^q = \frac{\|\mathbf{v}_{Re}^q\|^2 - k_{1Re}^2}{\left\|\mathbf{r}_{R_pe0}^q\right\|} \quad (10)$$

$$k_{3Te} = -3\frac{k_{1Te}k_{2Te}}{\left\|\mathbf{r}_{T_pe0}\right\|}, k_{3Re}^q = -3\frac{k_{1Re}^q k_{2Re}^q}{\left\|\mathbf{r}_{R_pe0}^q\right\|}\ldots \quad (11)$$

The ideal range history is the same way as (7)–(11), except that $\mathbf{v}_{Te}$ and $\mathbf{v}_{Re}^q$ is replaced by $\mathbf{v}_T$ and $\mathbf{v}_R^q$ respectively, as well as $\mathbf{r}_{T_pe0}$ and $\mathbf{r}_{R_pe0}^q$ is replaced by $\mathbf{r}_{T_p0}$ and $\mathbf{r}_{R_p0}^q$, separately. Hence, the ideal range history can be expressed as

$$R^q(\eta;\mathbf{r}_p) = \left\|\mathbf{r}_{T_p0}\right\| + \left\|\mathbf{r}_{R_p0}^q\right\| + \sum_{n=1}^{\infty}\frac{1}{n!}\left(k_{nT} + k_{nR}\right)\eta^n. \quad (12)$$

From (3), the echo delay is given by (13). Meanwhile, the Doppler frequency $f_d(\eta)$ is obtained from the Doppler phase $\phi_d(\eta)$ of the echo and denoted as (14)

$$\tau_d(\eta) = \frac{R^q(\eta;\mathbf{r}_p)}{c}^{\langle 1 \rangle} + \frac{\Delta R_e^q(\eta;\mathbf{r}_p)}{c}^{\langle 2 \rangle} - \Delta t^q(\eta)^{\langle 3 \rangle} \quad (13)$$

$$f_d(\eta) = \frac{\mathrm{d}\phi_d(\eta)}{2\pi\mathrm{d}\eta} = -\frac{\mathrm{d}R^q(\eta;\mathbf{r}_p)}{\lambda\mathrm{d}\eta}^{\langle 1 \rangle} - \frac{\mathrm{d}\Delta R_e^q(\eta;\mathbf{r}_p)}{\lambda\mathrm{d}\eta}^{\langle 2 \rangle} - f_c\left(\mu_0^q + 2\mu_1^q\eta + 3\mu_2^q\eta^2\right)^{\langle 3 \rangle}. \quad (14)$$

Term $\langle 1 \rangle$ in (13) and (14) denote the theoretical echo delay $\tau_i(\eta)$ and Doppler frequency $f_{d_i}(\eta)$, respectively. The echo delay components and Doppler frequency components from

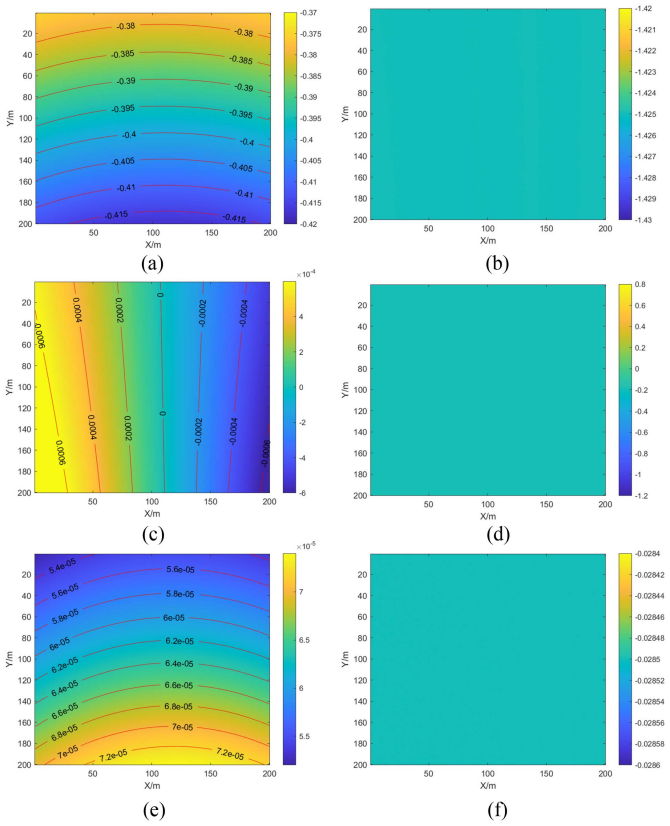

Fig. 3. Simulation of Doppler frequency for targets at different locations. DC introduced by (a) geometry error and (b) synchronization error. DFR introduced by (c) geometry error and (d) synchronization error. Third-order frequency introduced by (e) geometry error and (f) synchronization error.

geometry are the term $\langle 2 \rangle$, denoted as $\tau_g(\eta)$ and $f_{d_g}(\eta)$. In contrast, $\tau_s(\eta)$ and $f_{d_s}(\eta)$ denote the two components introduced by synchronization error. From the Doppler frequency, the Doppler centroid (DC) $f^q_{\mathrm{dc}_e}$, Doppler frequency rate (DFR) $f^q_{dr_e}$, and Doppler frequency rate of change (DFC) $f^q_{dt_e}$ can be further obtained as

$$\begin{cases} \tau_e(\eta) = \frac{\Delta R^q_e(\eta;\mathbf{r}_p)}{c} + \mu^q_0\eta + \frac{1}{2}\mu^q_1\eta^2 + \frac{1}{3}\mu^q_2\eta^3 \\ f^q_{\mathrm{dc}_e} = \frac{(k_{1Te}+k^q_{1Re})-(k_{1T}+k^q_{1R})}{\lambda} - f_c\mu^q_0 \\ f^q_{dr_e} = \frac{(k_{2Te}+k^q_{2Re})-(k_{2T}+k^q_{2R})}{\lambda} - 2f_c\mu^q_1 \\ f^q_{dt_e} = \frac{(k_{3Te}+k^q_{3Re})-(k_{3T}+k^q_{3R})}{2\lambda} - 6f_c\mu^q_2 \end{cases} \tag{15}$$

where $\Delta R^q_e(\eta;\mathbf{r}_p) = R^q_e(\eta;\mathbf{r}_p) - R^q(\eta;\mathbf{r}_p)$.

According to the preceding analysis, this section gives the characteristics of the geometry error and synchronization error in the echo delay and the Doppler frequency of each order parameter, as shown in Fig. 3. For targets at different locations in the same scene, the variation characteristics of DC, DFR, and DFC introduced by geometry error are analyzed separately in Fig. 3(a), (c), and (e). It can be seen that each order parameter varies with the change in the target position, combined with (15), it is concluded that DC, DFR, and DFC introduced by geometry error are spatial variants. In contrast, each order parameter of the Doppler frequency brought by the synchronization error is shown in Fig. 3(b), (d), and (f); the difference in target position does not affect the variation of each order parameter, which can be observed that the synchronization error is spatial invariant. Consequently, in this article, the decoupling of the two errors is realized based on the spatial variance of the geometry error and the spatial invariance of the synchronization error.

III. Proposed Method

According to the analysis, the actual Doppler frequency and time delay at any point in the echo consists of three components: the theoretical component, the geometry error component, and the synchronization error component. The theoretical component can be calculated based on the system parameters and the target position. For geometry error and synchronization error components, the better the estimated results, the nearer the actual Doppler frequencies and time delay are to the real values. For a point in the scene, the practical Doppler frequency and time delay can be calculated based on the energy trajectory of the echo and the reference time delay.

Therefore, the problem of error estimation can be converted into an optimization problem, with the objective of finding the optimal geometry and synchronization errors so as to minimize the discrepancy between the estimated versus the actual values of the Doppler frequencies and time delay, which realizes the decoupling of the geometry and synchronization errors.

Based on this, this article proposes an error estimation method for imaging that achieves decoupling of the geometry and synchronization errors of the echo from each receiver. The subimaging results after compensating the errors are then coherently superimposed. The implementation process of the proposed method can be divided into three parts as follows.

First, the energy trajectories of isolated strong points in each receiver echo are extracted to calculate the actual values of Doppler frequency and time delay. Second, an objective function is established to optimally solve the geometry and synchronization error to realize the decoupling, and the BP algorithm is used to obtain the imaging results of each receiver after compensating the error by phase factors constructed by the decoupled error estimations. Finally, the fusion of imaging results from multiple receivers yields a multistatic SAR high-precision imaging result. The specific implementation process of the algorithm is described in detail, which is shown in Fig. 4.

A. Time Delay Extraction and Parameter Estimation

Since the geometry error is spatial variant along the range, multiple energy trajectories need to be extracted to avoid falling into a local optimum when optimizing the objective function. It is set to extract $K(K \geq 3)$ isolated strong-point energy trajectories in each pair of any transceiver station echo.

1) Range History Inversion: For the $k(k = 1, 2, \ldots, K)$ energy trajectories, multiple strong points on the trajectory are selected for second-order fitting to obtain the range cell $E_k(\eta)$ where the trajectory is located.

Meanwhile, the search range $[E_k(\eta) - \Delta d/2, E_k(\eta) + \Delta d/2]$ is set for each azimuthal moment of this trajectory in the echo, where Δd is a constant, and the range cell with the strongest energy in the current azimuthal moment $E_{\mathrm{km}}(\eta)$ is

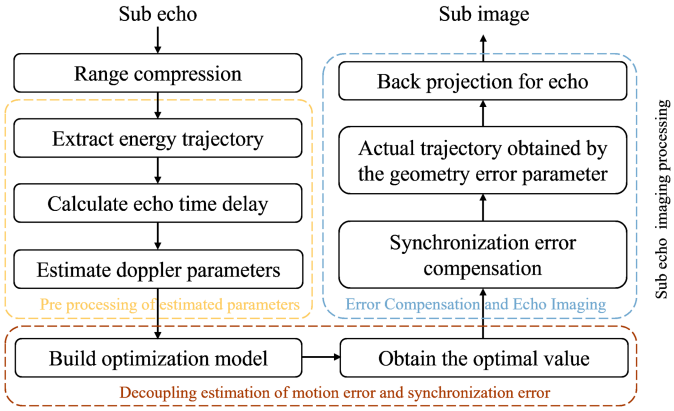

Fig. 4. Flowchart of decoupling compensation method of geometry error and synchronization error-based on optimization problem.

picked, which is calculated to get the actual delay of the scattering point $P_k(x_k, y_k)$ corresponding to this energy trajectory by the following:

$$\tau_k(\eta) = E_{\mathrm{km}}(\eta) \cdot dr/c - \tau_r \tag{16}$$

where dr is the range cell scale and τ_r is the reference delay.

2) Doppler Parameters Estimation: DFC $\hat{f}_{dt}(x_k, y_k)$ is estimated and compensated for the kth energy trajectory by using a parameter estimation approach Radon-cubic phase function (CPF)-Fourier transform (RCFT) in [3]. An FRFT-based parameter estimation method proposed by [30] is used to estimate DC $\hat{f}_{dc}(x_k, y_k)$ and DFR $\hat{f}_{dr}(x_k, y_k)$. Higher order parameters can be obtained by the corresponding methods.

B. Decoupling and Estimation of Geometry Error and Synchronization Error

The effects of geometry and time-frequency synchronization errors on the Doppler frequency and time delay are analyzed in (13) and (14), respectively, and the parameter optimization model is built using these relationships, starting by defining the unknowns for envelope and phase compensation of the echo into a solution vector

$$\Lambda = [\Delta e_T, \Delta e_R^q, \alpha_T, \alpha_R^q, \beta_T, \beta_R^q, \mu_0^q, \mu_1^q, \mu_2^q]\,. \tag{17}$$

Denote the target position of the kth extracted energy trajectory as $P_k(x_k, y_k, 0)$, combined with the reference time delay and Section III-A, the actual echo delay and Doppler parameters of each order for this point can be derived, which are expressed as functions $\tau_e(\Lambda, \eta; x_k, y_k)$, $f_{dc}(\Lambda; x_k, y_k)$, $f_{dr}(\Lambda; x_k, y_k)$, $f_{dt}(\Lambda; x_k, y_k)$, etc, related to the solution vector Λ and slow time η. For this energy trajectory, if a variable $\hat{\Lambda} = \Lambda$ exists that satisfying the relation

$$\begin{cases} \tau_e(\hat{\Lambda}, \eta; x_k, y_k) = \hat{\tau}_e(\eta; x_k, y_k) + \Delta\tau_k \\ f_{dc}(\hat{\Lambda}; x_k, y_k) = \hat{f}_{dc}(x_k, y_k) + \Delta f_{dc_k} \\ f_{dr}(\hat{\Lambda}; x_k, y_k) = \hat{f}_{dr}(x_k, y_k) + \Delta f_{dr_k} \\ f_{dt}(\hat{\Lambda}; x_k, y_k) = \hat{f}_{dt}(x_k, y_k) + \Delta f_{dt_k} \\ \dots \end{cases}. \tag{18}$$

Moreover, when $\Delta R_k, \Delta f_{dc_k}, \Delta f_{dr_k}$, and Δf_{dt_k} all converge to 0, it implies that the range history and Doppler parameter estimates of each order in the relation are nearer to the value. In order to quantitatively measure the accuracy of the individual estimation solutions, the evaluation functions of the kth energy trajectory are constructed separately

$$\begin{cases} \Phi_{\tau_k} = \left|\tau_e(\hat{\Lambda}, \eta; x_k, y_k) - \hat{\tau}_e(\eta; x_k, y_k)\right| \\ \Phi_{dc_k} = \left|f_{dc}(\hat{\Lambda}; x_k, y_k) - \hat{f}_{dc}(x_k, y_k)\right| \\ \Phi_{dr_k} = \left|f_{dr}(\hat{\Lambda}; x_k, y_k) - \hat{f}_{dr}(x_k, y_k)\right| \\ \Phi_{dt_k} = \left|f_{dt}(\hat{\Lambda}; x_k, y_k) - \hat{f}_{dt}(x_k, y_k)\right| \\ \dots \end{cases}. \tag{19}$$

Four evaluation functions containing the same solution vectors are constructed concerning Λ according to the minimum-maximum criterion

$$\Phi_k(\hat{\Lambda}) = \max\left\{\Phi_{\tau_k}, \Phi_{dc_k}, \Phi_{dr_k}, \Phi_{dt_k}\right\}. \tag{20}$$

To accelerate the convergence of the algorithm and avoid falling into local optimal solutions at the same time, the extracted multiple energy trajectories are integrated to construct the build-objective optimization function

$$\hat{\Lambda} = \arg\min_{\Lambda} \max\left\{\Phi_1(\Lambda), \Phi_2(\Lambda), \dots, \Phi_K(\Lambda)\right\}. \tag{21}$$

Aiming to solve this optimization model, the DE algorithm is utilized in this article to find the optimal solution. The DE algorithm is a stochastic heuristic search algorithm that randomly generates the initial population before iteration, constructs variant individuals through the individual differences of the current population, and then perturbs the new individuals under random deviation, with individual fitness as the selection criterion [31]. Accordingly, the DE algorithm has a favorable global optimal seeking ability by directing the search process to approximate the global optimal solution. In addition, it can solve the optimal solution in multidimensional space, making it a multiobjective optimization algorithm. And the algorithm flow is shown as Algorithm 1.

After the iteration convergence, the optimal solution of the optimization model is obtained as follows.

$$\hat{\Lambda} = \left[\Delta\hat{e_T}, \Delta\hat{e}_R^q, \hat{\alpha_T}, \hat{\alpha}_R^q, \hat{\beta_T}, \hat{\beta}_R^q, \hat{\mu_0^q}, \hat{\mu_1^q}, \hat{\mu_2^q}\right]. \tag{22}$$

So far, the purpose of decoupling the geometry error and synchronization error is achieved.

C. Error Compensation and Imaging

After decoupling, geometry error and synchronization error can be compensated and imaged according to Fig. 5.

1) The optimal solution $\hat{\Lambda}^q$ is utilized to construct phase factors showing in (23) to compensate for the errors caused by time and frequency synchronization error in the echo obtained by receiver q. H_T and H_F are compensated for time-delayed and Doppler, respectively

$$\begin{cases} H_F = \exp\left\{j2\pi f_T(\hat{\mu_0^q} + \hat{\mu_1^q}\eta + \hat{\mu_2^q}\eta^2)\eta\right\} \\ H_T = \exp\left\{j2\pi(\hat{\mu_0^q}\eta + \frac{1}{2}\hat{\mu_1^q}\eta^2 + \frac{1}{3}\hat{\mu_2^q}\eta^3)f_\tau\right\} \end{cases}. \tag{23}$$

2) The actual trajectory is obtained based on (5) and denoted as (24), which is utilized to image with the BP algorithm after

Algorithm 1: Optimal Solution Search Algorithm for Decoupling Geometry Error and Synchronization Error of Strong Point Trajectory.

INPUT: population size P, variables D, generations G_m, crossover factor CR, variation factor F_0.

Processing:

Step 1: Generate the randomly initialized population.

The upper bound of the individual variable is: $x_j^{(u)}$ while the lower bound is: $x_j^{(l)}$. The initial individual is represented as:

$x_{ji}^0 = r_{ji} \cdot (x_j^{(u)} - x_j^{(l)}) + x_j^{(l)}, i = 1, 2, \ldots, P, j = 1, 2, \ldots, D$

where r_{ji} is the uniform random number between [0,1] when generating individual x_{ji}^0.

Step 2: Represent the current population.

The current generation is G:

$S^G = \{X_i^G | X_i^G = (x_{1,i}, x_{2,i}, \ldots, x_{j,i}, \ldots, x_{D,i})\}$

Step 3: Mutation operator.

Calculate adaptive mutation factor:

$F = F_0 \times \exp\{\frac{1-G}{G_m+1-G}\}$,

where F determines the amplification ratio of the deviation vector.

The mutation vector is generated from the parent difference vector. Perform the following mutation operations on each individual:

$V_i = X_{v_1}^G + F \cdot (X_{v_2}^G - X_{v_3}^G)$

where $X_{v_1}^G, X_{v_2}^G$, and $X_{v_3}^G$ represent three randomly selected individuals that satisfying $i \neq v_1 \neq v_2 \neq v_3$.

Step 4: Crossover operator.

Constrain the cross-ratio of parent and mutation vectors. Generate D random numbers $r_j (j = 0, 1, \ldots, D)$ in the range [0,1] and determine whether the test population is composed of V_i or X_i^G based on the following equation:

$$c_{j,i} = \begin{cases} v_{j,i}, r_j \leq CR \\ x_{j,i}^G, otherwise \end{cases}$$

Step 5: Selection operator.

Selecting individuals with lower objective function values val to enter the next generation population:

$$X_i^{G+1} = \begin{cases} C_i, val(C_i) \leq val(X_i^G) \\ X_i^G, otherwise \end{cases}$$

Step 6: Termination conditions.

If $G = G_m$ or the optimal fitness $f_{best}(G)$ meets the accuracy requirements, terminate the generation and return the individual X corresponding to $f_{best}(G)$. Otherwise, make $G = G + 1$ and continue with step 2 to enter the next generation.

compensating for the synchronization error

$$\begin{cases} \mathbf{r_{Te}}(\eta) = \mathbf{r_T}(\eta)\mathbf{\Phi}(\hat{\alpha_T})\mathbf{\Psi}(\hat{\beta_T}) + \mathbf{\Delta e_T} \\ \mathbf{r}_{Re}^q(\eta) = \mathbf{r}_R^q(\eta)\Phi(\hat{\alpha}_R^q)\Psi(\hat{\beta}_R^q) + \Delta\hat{e}_R^q \end{cases} . \quad (24)$$

3) For every transceiver platform, 1) and 2) were exploited to acquire the subimaging results, and the final high-resolution imaging result is coherently superimposed on all subimaging results.

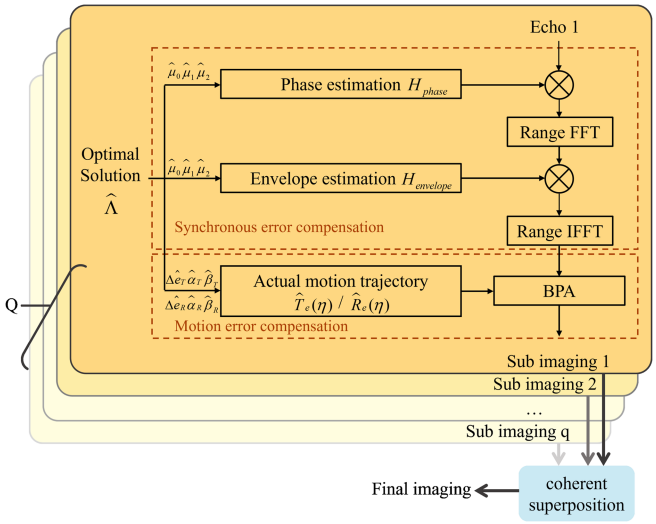

Fig. 5. Flowchart for error compensation and imaging.

TABLE I
SIMULATION PARAMETERS

Parameter	Symbol	Value
Carrier frequency	f_c	9.5 GHz
Pulse width	T_p	1 us
Pulse repetition frequency	PRF	1 kHz
Bandwidth	B_r	600 MHz
Transmitter coordinate	$\mathbf{r}_{T0}$	(500,0,500)m
Receiver 1 coordinate	$\mathbf{r}_{R0}^1$	(500,50,500)m
Receiver 2 coordinate	$\mathbf{r}_{R0}^2$	(500,70,500)m
Receiver 3 coordinate	$\mathbf{r}_{R0}^3$	(500,90,500)m

IV. RESULTS

To verify the effectiveness of the proposed method, experiments of point targets and real SAR scenarios are conducted with multistatic SAR simulation data to realize the decoupling of the geometry and synchronization errors. The imaging results of all the receiver echoes are coherently superimposed to obtain high-precision SAR images and improve the imaging frame rate. In addition to the process of utilizing BP algorithm imaging with autofocus method in [32] (BP+AF), two methods are compared with the proposed approach to demonstrate the superiority of the latter. 1) Method I: Compensate synchronization error for distributed SAR [28]. 2) Method II: Calculate the flight trajectory by exploiting the Doppler phase error in [24] to compensate for motion error. The simulation parameters are indicated in Table I.

A. Point Target Simulation

Point target simulation is first carried out to verify the capability of the presented approach. In this simulation, 25 stationary targets are generated in the scene, whose distribution in space is indicated in Fig. 6, and the platform flight velocity vectors are all (0, 4, 0) m/s. The process of extracting the energy trajectory of the isolated strong point is shown in Fig. 7, where several points

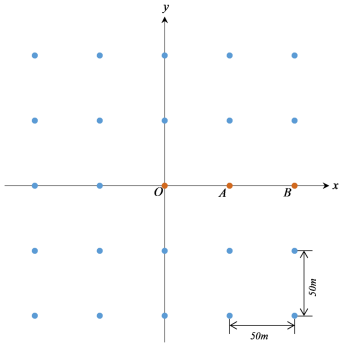

Fig. 6. Spatial distribution of point targets.

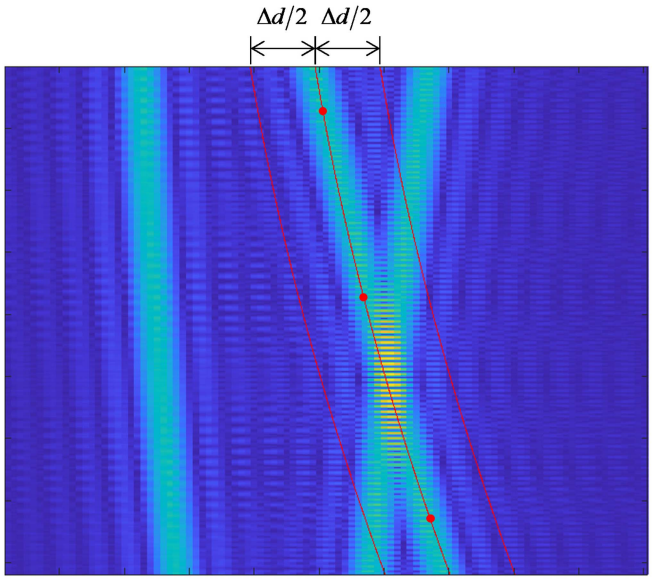

Fig. 7. Process of extracting isolated strong-point energy trajectories.

on the energy trajectory are taken and fitted to calculate the range cell migration momentum at each azimuthal moment. To obtain an accurate trajectory, strong points can be taken within a certain range around the fitted line and fitted again. After extracting the trajectory the proposed method can be utilized to decouple the error. The imaging result is shown in Fig. 8. It can be observed that by BP+AF, point O is used as a reference point to calculate the compensated phase, which has a decent focus after compensation, but the rest of the points are poorly focused. Method I implements frequency synchronization and rough time synchronization by direct wave and establishes an optimization model based on image entropy, whose optimization results compensate for the residual time synchronization error, thus obtaining good focused results of 2-D images. However, the method only considers the synchronization error between platforms; the geometry error still exists, while the estimation results obtained by minimizing the image entropy can only solve the spatial invariant error when compensating for the geometry error, and the spatial variant error remains. Method II calculates the geometry trajectory from the Doppler phase, where the

TABLE II
ESTIMATION ERROR OF SYNCHRONIZATION ERROR AND GEOMETRY ERROR

error type	Maximum estimation error		
	Receiver 1	Receiver 2	Receiver 3
$\Delta f_{\max}$	0.0652	0.0152	0.0145
$\Delta T_{\max}$	0.0022	0.0005	0.0003
range history	0.0032	0.0037	0.0035

reference point target O could obtain a better-focusing result. However, on account of considering synchronization error as a spatial variant error, it will lead to the out of focus of the points that are far away from the reference target, such as A, B. For comparison, the proposed method could effectively decouple the geometry error and synchronization error and compensate for them separately. It also solves the problems of side lobe widening and position drift, obtaining a high-precision imaging result.

In addition, the estimation error of the geometry error and synchronization error is shown in Table II. $\Delta f_{\max}$, $\Delta T_{\max}$ denote the estimation error of the frequency synchronization error and time synchronization error, respectively. From the table, it can be calculated that the phase error satisfies $|2\pi\Delta f_{\max}| \leq \pi/4$, and the enveloping error satisfies $|2\pi\Delta R/\lambda| \leq \pi/4$, which verifies the validity of the method in this article.

In order to quantitatively assess the imaging quality of the different methods, the azimuth profiles of point targets at different positions are represented in Fig. 9. and the metrics, which include resolution, peak sidelobe ratio (PSLR), and integrated sidelobe ratio of these targets are measured separately and shown in Table III. Among them, the imaging results before geometry error and synchronization error decoupling are poor. Therefore, their PSLR, ISLR, and resolution are not listed in the table. From the metrics, it can be concluded that geometry error that is not compensated for in Method I can cause the final imaging result to be defocused, there are few points with good performances in BP+AF, and there is a significant variation between the focusing effects of points at different locations. Even though Method II can focus the partial scene well, the rest of the targets at different positions have various degrees of defocusing. Even though the performance of the proposed method in terms of PSLR and ISLR is slightly worse than the theoretical values, it can focus the target well in the whole scene.

B. Real SAR Scenario

In addition, this article also proves the effectiveness of the algorithms by processing the real SAR scenario data, the scene size is set as $100\,\text{m} \times 100\,\text{m}$.

1) Case I: The system parameters are listed in Table I, and the imaging results under different algorithms are shown in Fig. 10.

Intending to quantitatively describe the performance of the methods, the imaging quality of different algorithms needs to be specifically measured, and the three indexes namely, sharpness,

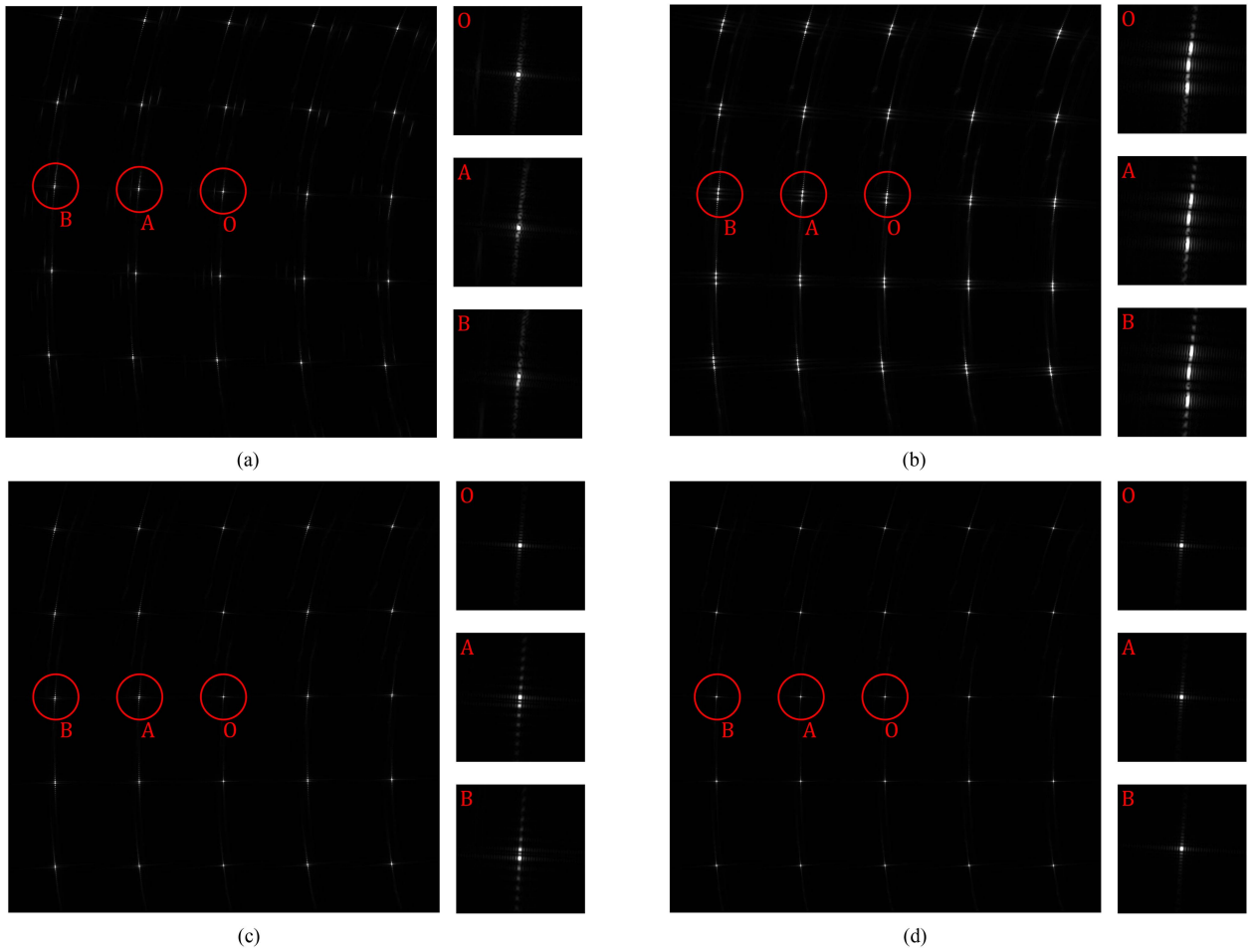

Fig. 8. Imaging results of point targets with different algorithms. (a) BP+AF. (b) Method I. (c) Method II. (d) Proposed method.

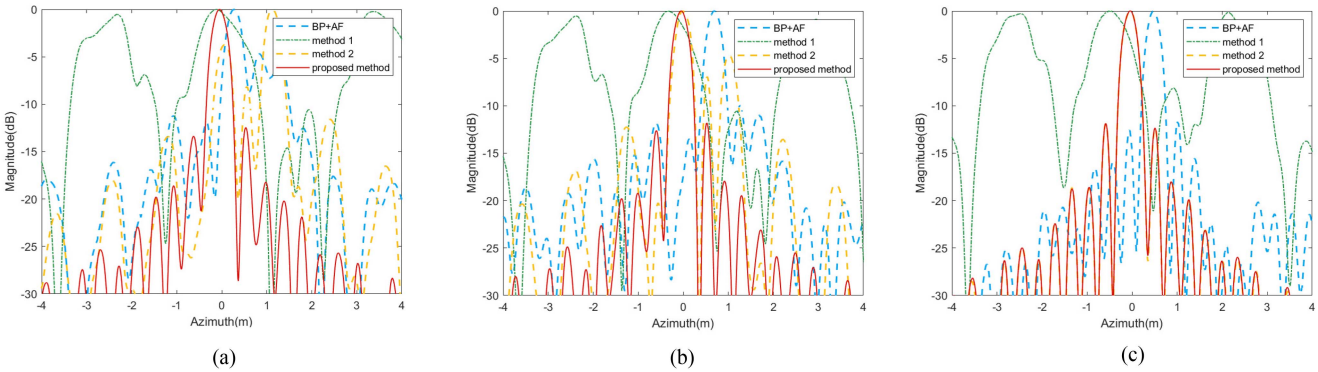

Fig. 9. Azimuth profiles of point targets with different positions. (a) Point B. (b) Point A. (c) Point O.

TABLE III
MEASURED IMAGING METRICS FOR THE THREE SCATTERS IN THE POINT TARGETS SIMULATION

Point Target	BP+AF			Method I			Method II			Proposed method		
	PSLR (dB)	ISLR (dB)	Resolution (cm)	PSLR (dB)	ISLR (dB)	Resolution (cm)	PSLR (dB)	ISLR (dB)	Resolution (cm)	PSLR (dB)	ISLR (dB)	Resolution (cm)
A	–5.37	–0.90	0.37	–0.50	3.04	0.93	–8.14	–1.73	0.35	–12.46	–10.37	0.37
B	–9.96	–4.88	0.36	–0.53	3.02	0.81	–6.92	–2.70	0.35	–11.81	–10.38	0.35
O	–1 .68	–8.53	0.32	–0.33	3.67	0.81	–1 .90	–1 .40	0.33	–11.86	–10.36	0.33

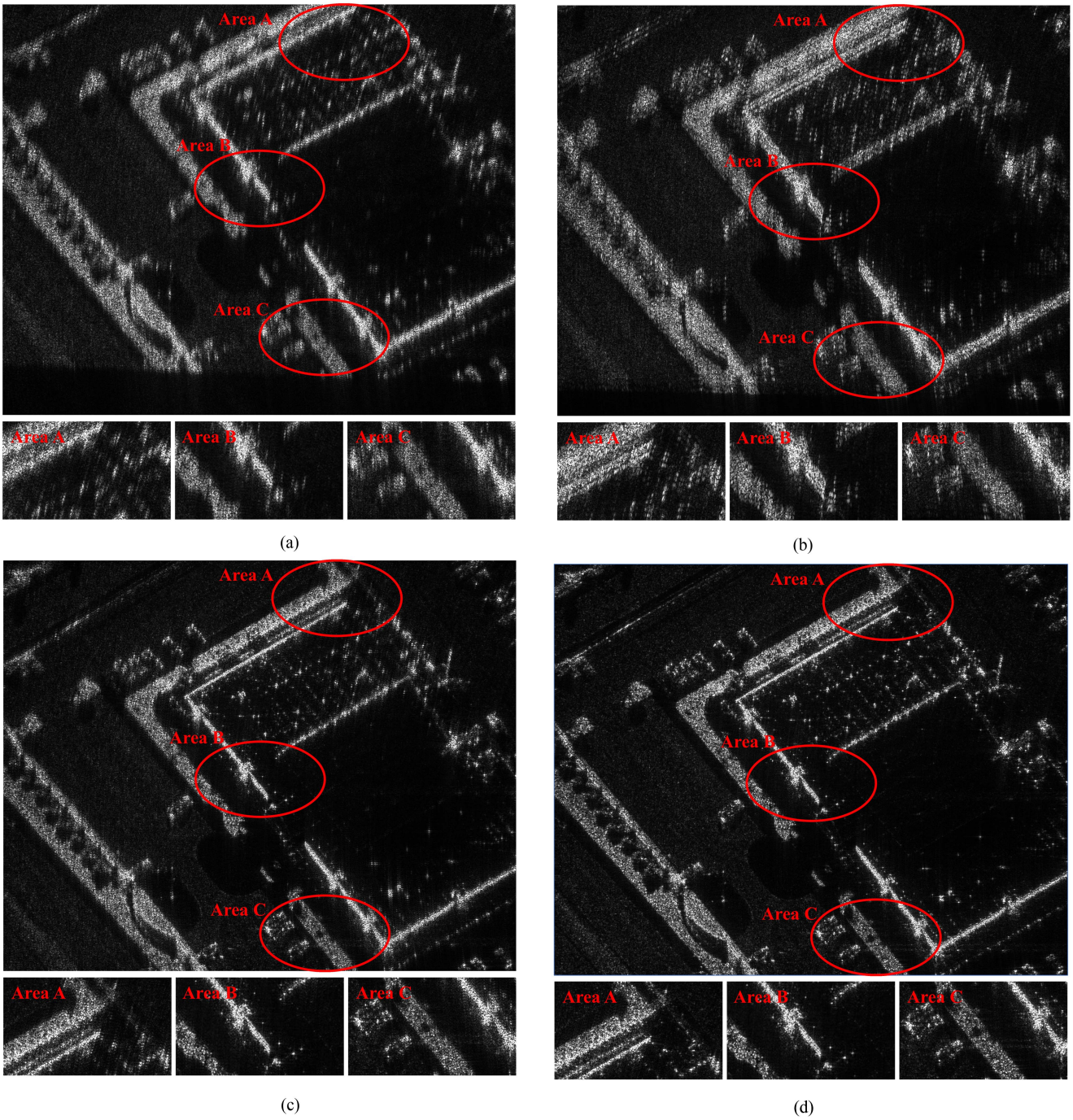

Fig. 10. Imaging results of different methods for the real SAR scenario I with three receivers. (a) BP+AF. (b) Method I. (c) Method II. (d) Proposed method.

TABLE IV
MEASURED IMAGING METRICS FOR THE SCENARIO I

	BP+AF	Method I	Method II	Proposed method
Sharpness	1.0000	0.9283	1.5599	**1.8281**
Entropy	1.0000	1.0077	0.9850	**0.9763**
Contrast	1.0000	0.9983	1.0089	**1.0121**

The bold values emphasize the validity of the proposed methodology.

entropy and contrast of the image are given in Table IV. For ease of comparison, the metrics are listed in relative values, set to 1 for imaging results without compensation.

In terms of metrics, the proposed method has the highest contrast and sharpness and the lowest entropy, indicating optimal image quality, with Method II coming in second. Thus allowing us to obtain that the imaging results of the BP+AF and Method I are defocused obviously. From the results of Method I, although the linear term of geometry error remains after compensating the synchronization error, it cannot solve the problem of positional offset because it compensates the residual synchronization error by minimizing the entropy, and the difference in imaging position leads to serious defocusing in final imaging. While Method II focuses marginal parts much worse than the center reference point, the degree of focusing is also spatial variant.

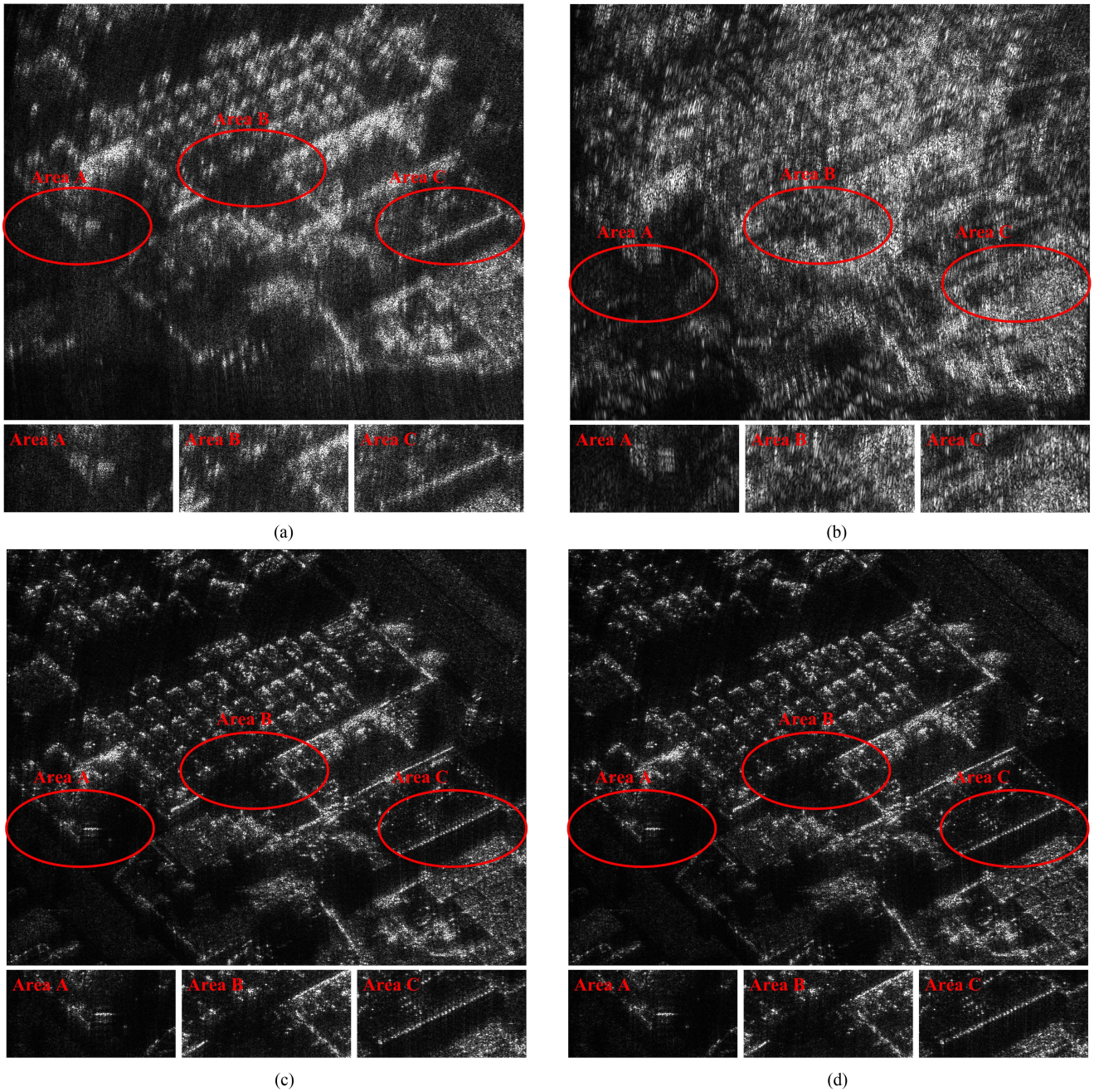

Fig. 11. Imaging results of different methods for the real SAR scenario II with eight receivers. (a) BP+AF. (b) Method I. (c) Method II. (d) Proposed method.

In contrast, the proposed method performs well in all three metrics.

2) Case II: In addition, this article increases the number of receiver platforms to eight, with the x and z coordinates of the position at the initial moment of time being invariant, and the y coordinates are changed to 39, 47, 54, 62, 70, 77, 85, and 93 m. The effectiveness of the algorithms is also proved by processing real SAR scene data, and the imaging results are shown in Fig. 11. Similarly, the measurements are in the Table V.

TABLE V
MEASURED IMAGING METRICS FOR THE SCENARIO II

	BP+AF	Method I	Method II	Proposed method
Sharpness	1.0000	0.3519	3.1112	**3.3479**
Entropy	1.0000	1.0174	0.9647	**0.9615**
Contrast	1.0000	0.9777	1.0238	**1.0253**

The bold values emphasize the validity of the proposed methodology.

Comparing the imaging results of Scene I, it can be seen that in Scene II, the imaging results of BP+AF are less satisfactory. The defocusing of Method I is much more severe due to the number of receivers increasing. The geometry error results in uncorrected positional offsets of the targets, which cannot be focused well in the final imaging. Whereas Method II focuses well in area B, the center of the scene, areas A and C, far away from area

B, are still out of focus. In contrast, the proposed method can have well-focused results for the whole scene, which verifies the effectiveness of the proposed method.

V. Conclusion

In order to realize high-precision multistatic SAR imaging under the coupling of synchronization error and geometry error, this article proposes a novel multistatic SAR imaging method with decoupling of synchronization error and geometry error. First, the characterization of spatial variation of the two errors is analyzed. Then a constrained optimization model is established based on their effects on the Doppler frequency and time delay, followed by obtaining the optimization results with the DE algorithm. Finally, the errors are compensated and coherently superimposed with all subimaging results. Compared with the traditional method of compensating for only one of the errors, this method can simultaneously estimate the synchronization error and geometry error, and good imaging results can be obtained after using the estimated values for compensation. The results based on point targets and real SAR scenarios show that the method has better estimation results than the traditional step-by-step error compensation method.

References

[1] H. An, J. Wu, Z. Sun, J. Yang, Y. Huang, and H. Yang, "Topology design for geosynchronous spaceborne–airborne multistatic SAR," *IEEE Geosci. Remote Sens. Lett.*, vol. 15, no. 11, pp. 1715–1719, Nov. 2018.

[2] G. Qian and Y. Wang, "Monostatic-equivalent algorithm via Taylor expansion for BiSAR ship target imaging," *IEEE Trans. Geosci. Remote Sens.*, vol. 61, 2022, Art. no. 5200919.

[3] C. Zeng, D. Li, X. Luo, D. Song, H. Liu, and J. Su, "Ground maneuvering targets imaging for synthetic aperture radar based on second-order keystone transform and high-order motion parameter estimation," *IEEE J. Sel. Topics Appl. Earth Observ. Remote Sens.*, vol. 12, no. 11, pp. 4486–4501, Nov. 2019.

[4] C. Huang, Z. Li, H. An, Z. Sun, J. Wu, and J. Yang, "Optimal GNSS-based passive SAR large field-of-view imaging via multistatic configuration: Method and experimental validation," *IEEE J. Sel. Topics Appl. Earth Observ. Remote Sens.*, vol. 15, pp. 9873–9884, 2022.

[5] H. Ren et al., "A hybrid resolution enhancement framework for swarm UAV SAR based on cost-effective formation strategy," *IEEE Trans. Geosci. Remote Sens.*, vol. 62, 2023, Art. no. 5200216.

[6] W. Pu, "SAE-Net: A. deep neural network for SAR autofocus," *IEEE Trans. Geosci. Remote Sens.*, vol. 60, 2022, Art. no. 5220714.

[7] Y. Song, W. Pu, J. Huo, J. Wu, Z. Li, and J. Yang, "Deep parametric imaging for bistatic SAR: Model, property and approach," *IEEE Trans. Geosci. Remote Sens.*, vol. 62, 2024, Art. no. 5212416.

[8] J. Wu, W. Pu, H. An, Y. Huang, H. Yang, and J. Yang, "Learning-based high-frame-rate SAR imaging," *IEEE Trans. Geosci. Remote Sens.*, vol. 61, 2023, Art. no. 5208813.

[9] L. Fan, H. Wang, Q. Yang, Y. Wang, B. Deng, and H. Xiao, "High frame-rate and low-latency video SAR based on robust Doppler parameters estimation in the terahertz regime," *IEEE Trans. Geosci. Remote Sens.*, vol. 61, 2023, Art. no. 5207016.

[10] J. Ding, L. Wen, C. Zhong, and O. Loffeld, "Video SAR moving target indication using deep neural network," *IEEE Trans. Geosci. Remote Sens.*, vol. 58, no. 10, pp. 7194–7204, Oct. 2020.

[11] W. Pu, X. Wang, J. Wu, Y. Huang, and J. Yang, "Video SAR imaging based on low-rank tensor recovery," *IEEE Trans. Neural Netw. Learn. Syst.*, vol. 32, no. 1, pp. 188–202, Jan. 2021.

[12] F. Zuo and J. Li, "A persistent imaging method for video-SAR in terahertz band," in *Proc. Int. Appl. Comput. Electromagn. Soc. Symp.*, 2017, pp. 1–2.

[13] J. Ding, K. Zhang, X. Huang, and Z. Xu, "High frame-rate imaging using swarm of UAV-borne radars," *IEEE Trans. Geosci. Remote Sens.*, vol. 62, 2024, Art. no. 5204912.

[14] H. Ren et al., "Swarm UAV SAR for 3-D imaging: System analysis and sensing matrix design," *IEEE Trans. Geosci. Remote Sens.*, vol. 60, 2022, Art. no. 5238316.

[15] H. Wang, X. Chen, S. C. Zheng, D. Yang, J. H. Mei, and S. L. Wu, "Analysis of spatial synchronization errors for spaceborne bistatic SAR system," in *Proc. 2nd China Int. SAR Symp.*, 2021, pp. 1–5.

[16] W.-Q. Wang, "GPS-based time & phase synchronization processing for distributed SAR," *IEEE Trans. Aerosp. Electron. Syst.*, vol. 45, no. 3, pp. 1040–1051, Jul. 2009.

[17] P. López-Dekker, J. J. Mallorqui, P. Serra-Morales, and J. Sanz-Marcos, "Phase synchronization and doppler centroid estimation in fixed receiver bistatic sar systems," *IEEE Trans. Geosci. Remote Sens.*, vol. 46, no. 11, pp. 3459–3471, Nov. 2008.

[18] S. Guo, G. Cui, L. Kong, Y. Song, and X. Yang, "Multipath analysis and exploitation for MIMO through-the-wall imaging radar," *IEEE J. Sel. Topics Appl. Earth Observ. Remote Sens.*, vol. 11, no. 10, pp. 3721–3731, Oct. 2018.

[19] D. Liang et al., "A high-accuracy synchronization phase-compensation method based on Kalman filter for bistatic synthetic aperture radar," *IEEE Geosci. Remote Sens. Lett.*, vol. 17, no. 10, pp. 1722–1726, Oct. 2020.

[20] P. Zhou, M. Sui, Z. Zhang, Y. Wang, X. Zhang, and J. Zhang, "Influence analysis of time synchronization error on altimetry accuracy of multibaseline SARs," *J. Appl. Remote Sens.*, vol. 15, no. 4, 2021, Art. no. 046509.

[21] Y. Ji et al., "Motion compensation method using direct wave signal for CTSR bistatic HFSWR," *IEEE Geosci. Remote Sens. Lett.*, vol. 20, 2023, Art. no. 3502005.

[22] W. Pu and Y. Bao, "RPCA-AENet: Clutter suppression and simultaneous stationary scene and moving targets imaging in the presence of motion errors," *IEEE Trans. Neural Netw. Learn. Syst.*, vol. 35, no. 2, pp. 2339–2352, Feb. 2024.

[23] Y. Hai et al., "Microwave photonic SAR high-precision imaging based on optimal subaperture division," *IEEE Trans. Geosci. Remote Sens.*, vol. 60, 2022, Art. no. 5232317.

[24] Y. Li, W. Li, J. Wu, Z. Sun, H. Sun, and J. Yang, "An estimation and compensation method for motion trajectory error in bistatic SAR," *Remote Sens.*, vol. 14, no. 21, 2022, Art. no. 5522.

[25] Y. Luomei and F. Xu, "Segmental aperture imaging algorithm for multirotor UAV-borne miniSAR," *IEEE Trans. Geosci. Remote Sens.*, vol. 61, 2023, Art. no. 5202318.

[26] Y. Zhang, S. Chang, R. Wang, and Y. Deng, "An innovative push-to-talk (PTT) synchronization scheme for distributed SAR," *IEEE Trans. Geosci. Remote Sens.*, vol. 60, 2021, Art. no. 5213313.

[27] W. Li, D. Zou, Y. Li, Z. Liu, Z. Li, and J. Yang, "An estimation scheme of the linear time synchronization error for bistatic forward-looking SAR," in *Proc. IEEE Radar Conf.*, 2019, pp. 1–3.

[28] Y. Wang et al., "First demonstration of single-pass distributed SAR tomographic imaging with a p-band UAV SAR prototype," *IEEE Trans. Geosci. Remote Sens.*, vol. 60, 2022, Art. no. 5238618.

[29] Y. Li, W. Li, Z. Li, J. Wu, Y. Huang, and J. Yang, "Frequency reference error analysis for bistatic SAR," in *Proc. IGARSS IEEE Int. Geosci. Remote Sens. Symp.*, 2019, pp. 3527–3530.

[30] Y. Zhao, H. Yu, G. Wei, F. Ji, and F. Chen, "Parameter estimation of wideband underwater acoustic multipath channels based on fractional fourier transform," *IEEE Trans. Signal Process.*, vol. 64, no. 20, pp. 5396–5408, Oct. 2016.

[31] R. Storn and K. Price, "Differential evolution–A simple and efficient heuristic for global optimization over continuous spaces," *J. Glob. Optim.*, vol. 11, pp. 341–359, 1997.

[32] J. N. Ash, "An autofocus method for backprojection imagery in synthetic aperture radar," *IEEE Geosci. Remote Sens. Lett.*, vol. 9, no. 1, pp. 104–108, Jan. 2012.

Wanmin Wu (Student Member, IEEE) received the B.S. degree in electronic engineering in 2020, from Sichuan University (SCU), Chengdu, China, where she is currently working toward the Ph.D. degree in information and communication engineering with the School of Information and Communication Engineering, University of Electronic Science and Technology of China (UESTC), Chengdu, China.

Her research interests include synthetic aperture radar imaging and ship target imaging.

Wei Pu (Member, IEEE) received the B.S. and Ph.D. degrees in electronic engineering from the University of Electronic Science and Technology of China (UESTC), Chengdu, China, in 2012 and 2018, respectively.

From 2017 to 2018, he was a Visiting Student with the Department of Electrical Engineering, Columbia University, New York, NY, USA. From 2019 to 2022, he was a Research Fellow with University College London (UCL), London, U.K. He is currently a Professor with UESTC. His research interests include synthetic aperture radar, sparse signal processing, and deep learning.

Dr. Pu was a recipient of the Newton International Fellowship from the Royal Society, U.K.

Junjie Wu (Senior Member, IEEE) received the B.S., M.S., and Ph.D. degrees in electronic engineering from University of Electronic Science and Technology of China (UESTC), Chengdu, China, in 2004, 2007, and 2013, respectively.

He is currently a Professor with the UESTC. From January 2012 to January 2013, he was a Visiting Student with the Department of Electrical and Computer Engineering, Duke University, USA. His research interests include synthetic aperture radar imaging (particular emphasis on bistatic synthetic aperture radar).

Dr. Wu is the Reviewer of IEEE TRANSACTIONS ON GEOSCIENCE AND REMOTE SENSING, IEEE TRANSACTIONS ON SIGNAL PROCESSING, *IEEE Journal of Selected Topics in Applied Earth Observations and Remote Sensing* (JSTARS), *Journal of Selected Topics in Signal Processing*, *IEEE Geoscience and Remote Sensing Letters* (GRS), *IET Radar Sonar and Navigation* (RSN), and so on.

Yu Hai (Student Member, IEEE) received the B.S. degree in electronic engineering in 2018, from the University of Electronic Science and Technology of China (UESTC), Chengdu, China, where he is currently working toward the Ph.D. degree in information and communication engineering with the School of Information and Communication Engineering.

From 2023 to 2024, he was a Visiting Student with the School of Electrical and Electronic Engineering, Nanyang Technological University, Singapore. His research interests include microwave photonic SAR/ISAR imaging and sparse signal recovery.

Xinyu Mao (Student Member, IEEE) received the B.S. degree in electronic engineering in 2019, from the University of Electronic Science and Technology of China (UESTC), Chengdu, China, where she is currently working toward the Ph.D. degree in information and communication engineering with the School of Information and Communication Engineering.

Her research interests include multistatic synthetic aperture radar imaging.

Hongyang An (Member, IEEE) received the B.S. and Ph.D. degrees in electronic engineering from the University of Electronic Science and Technology of China (UESTC), Chengdu, China, in 2015 and 2020, respectively.

From 2019 to 2020, he was a Visiting Student with Nanyang Technological University, Singapore. He is currently with UESTC. His research interests include synthetic aperture radar and sparse signal processing.

Zhongyu Li (Member, IEEE) received the B.S. and Ph.D. degrees in electronic engineering from the University of Electronic Science and Technology of China (UESTC), Chengdu, China, in 2011 and 2017, respectively.

From 2015 to 2016, he was a Visiting Ph.D. Student with the Department of Information Engineering, Electronics and Telecommunications, Sapienza University of Rome, Rome, Italy. He is currently a Research Professor with UESTC. He has authored or coauthored more than 70 journal articles and conference papers. His research interests include synthetic aperture radar (SAR) technology (particular emphasis on bistatic/multistatic SAR moving target detection and imaging technologies).

Dr. Li is the Winner of the 2022 URSI Young Scientists Award and the Outstanding Doctoral Society Award of the Chinese Institute of Electronics. He was successfully selected for the China Postdoctoral Innovative Talent Support Program. He received the Excellent Paper Award-First Prize at the 2019 6th APSAR. He has served on the editorial boards of Modern Radar and Radar Science and Technology. He has served as a Guest/Topic Editor for *Remote Sensing* and *Frontiers in Signal Processing*.